On the dynamical nature of the active center in a single-site photocatalyst visualized by 4D ultrafast electron microscopy

Byung-Kuk Yoo[a,1], Zixue Su[a,1], John Meurig Thomas[b], and Ahmed H. Zewail[a,2]

[a]Physical Biology Center for Ultrafast Science and Technology, Arthur Amos Noyes Laboratory of Chemical Physics, California Institute of Technology, Pasadena, CA 91125; and [b]Department of Materials Science and Metallurgy, University of Cambridge, Cambridge CB3 0FS, United Kingdom

Contributed by Ahmed H. Zewail, November 19, 2015 (sent for review November 4, 2015; reviewed by Oh-Hoon Kwon, Tobin J. Marks, and Hiromi Yamashita)

Understanding the dynamical nature of the catalytic active site embedded in complex systems at the atomic level is critical to developing efficient photocatalytic materials. Here, we report, using 4D ultrafast electron microscopy, the spatiotemporal behaviors of titanium and oxygen in a titanosilicate catalytic material. The observed changes in Bragg diffraction intensity with time at the specific lattice planes, and with a tilted geometry, provide the relaxation pathway: the $Ti^{4+}=O^{2-}$ double bond transformation to a $Ti^{3+}–O^{1-}$ single bond via the individual atomic displacements of the titanium and the apical oxygen. The dilation of the double bond is up to 0.8 Å and occurs on the femtosecond time scale. These findings suggest the direct catalytic involvement of the $Ti^{3+}–O^{1-}$ local structure, the significance of nonthermal processes at the reactive site, and the efficient photo-induced electron transfer that plays a pivotal role in many photocatalytic reactions.

ultrafast electron microscopy | single-site photocatalysis | titanium based photocatalyst | ulatrafast phenomena | time-resolved microscopy

Single-site catalysts of both the thermally and photoactivated kind now occupy a prominent place in industrial- and laboratory-scale heterogeneous catalysis (1–8). Among the most versatile of these are the ones consisting of coordinatively unsaturated transition metal ions (Ti, Cr, Fe, Mn. . .) that occupy substitutional sites in well-defined, three-dimensionally extended, open-structure silicates of the zeolite type. The well-known and most widely used are the 4- or 5-coordinated Ti(IV) ions accommodated within the crystalline phase of silica, silicalite (9–14).

Titanosilicates, especially, are used extensively both industrially and in the laboratory for a wide range of chemo-, regio-, and shape-selective oxidations of organic compounds (15–18). These single-site heterogeneous photocatalysts are quite distinct from those typified by TiO_2, $SrTiO_3$, and other titaniferous photocatalysts where the Ti(IV) ions are in 6-coordination; and where, in interpreting the processes involved in harnessing solar radiation, electronic band structure considerations hold sway in preference to the localized states (see, e.g., refs. 19, 20). It has been demonstrated (16–18, 21, 22) that single-site, coordinatively unsaturated Ti(IV)-centered photocatalysts are especially useful in the aerial oxidation of environmental pollutants in the photodegradation of NO (to N_2 and O_2), of H_2O (to H_2 and O_2), and in the photocatalytic reduction of CO_2 to yield methanol. There is an exigent need to explore the precise nature of the electronic, temporal, and spatial changes accompanying the initial act of photoabsorption that sets in train the ensuing elementary chemical processes that are of vital environmental significance in, for example, the utilization of anthropogenic CO_2 as a chemical feedstock (23).

Here, we report the use of 4D ultrafast electron microscopy (UEM) (24–26) to trace the spatiotemporal behavior of the Ti(IV) and O^{2-} ions at the photocatalytic active center in the structurally well-characterized titanosilicate $Na_4Ti_2Si_8O_{22}{\cdot}4H_2O$, known as JDF-L1 (27–29). JDF stands for Jilin–Davy–Faraday, as the crystalline solid described here was discovered and characterized in joint work involving Jilin University (P. R. China) and the Davy–Faraday Laboratory at the Royal Institution of Great Britain. L1 stands for the first layered catalyst formed during that collaboration; 5-coordinated solids containing Ti(IV) ions are rare among the hundred or so titaniferous minerals, the prime example being fresnoite, $Ba_2Ti_2Si_2O_8$. We choose this photocatalyst with 5-coordinated Ti because of its unique bonding structure. Our approach entails monitoring, at femtosecond resolution, the changes in intensities and anisotropies of Bragg (electron) diffraction reflections in such a manner as to retrieve the change in valency and the time scales involved in both the formation of $Ti^{3+}–O^{1-}$ bond and the relaxation of the energy back to the local structure of the Ti = O bond in JDF-L1. Through these diffraction studies, and the associated Debye–Waller effect and structural factors anisotropies, it is found that a $Ti^{3+}–O^{1-}$ bond is formed on the femtosecond time scale; whereas, the back relaxation from the site to the structure occurs on a much longer time scale, permitting ample time for reactivity involving $Ti^{3+}–O^{1-}$, and indicating the potential significance of nonthermal processes in the photocatalytic activity at the reactive site.

Materials and Methods

The hydrated, pristine JDF-L1 is hydrothermally synthesized using previous protocols (27). A microliter drop of aqueous JDF-L1 suspensions was deposited on the 200-mesh holey carbon TEM grid (Electron Microscopy Science), followed by drying in the air for 2–3 d. The as-prepared structure of the tetragonal phase could change into the dehydrated phase with lower symmetry, due to the irreversible loss of water, when ethanol was used to disperse the sample onto the TEM grid. However, enough solubilization in water enhances the stability of the pristine sample against the dehydration, thus hindering the irreversible phase change. We performed the time-resolved diffraction measurements and found that the initial phase did not change during the measurements under the optimized fluence.

Significance

The nature of the active site in (photo) catalysis is fundamental to our understanding of the processes involved, and to their control. Four-dimensional ultrafast electron microscopy (UEM) provides a dynamic probe for catalytic active site in photocatalytic materials thanks to its unprecedented resolution both in time (femtosecond) and space (angstrom). In this contribution, we visualize the femtosecond atomic movement at the titanium active center in a single-site photocatalyst. UEM allows us to investigate the structural dynamics of the radiation sensitive specimen by measuring time-resolved diffraction intensities from different lattice planes. These findings contribute fundamental insights for developing advanced photocatalysts and suggest broad ranges of applications.

Author contributions: B.-K.Y., Z.S., J.M.T., and A.H.Z. designed research; B.-K.Y. and Z.S. performed experiments; B.-K.Y. and Z.S. analyzed data; and B.-K.Y., Z.S., J.M.T., and A.H.Z. wrote the paper.

Reviewers: O.-H.K., Ulsan National Institute of Science and Technology; T.J.M., Northwestern University; and H.Y., Osaka University.

The authors declare no conflict of interest.

[1]B.-K.Y. and Z.S. contributed equally to this work.

[2]To whom correspondence should be addressed. Email: zewail@caltech.edu.

All measurements were performed using UEM-2 and the principle of the apparatus has been described elsewhere (30). The microscope adapts synchronized pulses of two different UV wavelengths: the 259-nm pulse to extract the probing photoelectrons produced from the cathode irradiation, and the 346-nm beam, which was shone on the specimen. Both pulses were generated from a 1,038-nm femtosecond infrared laser source operating at given repetition rate (in this case 100 kHz). By varying the optical delay line between the two laser pulses, a well-defined temporal delay was established and adjusted as needed. The pump beam has a fixed angle to the electron beam. The photon-induced near-field electron microscopy (PINEM) (31) interaction in a silver nanowire was used for in situ determination of time zero.

The diffraction images were acquired stroboscopically using up to six scans with a good signal-to-noise ratio. Pump beam characteristics were optimized on the specimen without any cumulative damage through data acquisition; the diameter of FWHM of ~40 μm and the fluence of about 1 mJ/cm^2 were used. The peak intensities obtained for each Bragg spot at a given time range were normalized to their respective (000) intensities. The temporal evolution of the normalized intensity for a given Bragg spot was fit using a convolution of an exponential decay and a Gaussian instrument response function. The former corresponds to the intrinsic response of the sample and the latter to the temporal resolution of the instrument.

Results and Discussion

In JDF-L1, the Ti(IV) ions are in a 5-coordinated square pyramidal arrangement, and there is one short Ti = O bond, parallel to the [001] zone axis, where the oxygen is situated at the apex of the pyramid. As depicted in the upper panel of Fig. 1, the noncentrosymmetric tetragonal layered structure of JDF-L1 contains one TiO_5 square pyramid (represented in blue) and four SiO_4 tetrahedra (in yellow). Two layers are sandwiched between two planes of Na^+ ions and water molecules. This small cage-type unit contains the titanium active center at its typical IV oxidation state. One oxygen atom out of the five Ti–O bonds is parallel to the [001] zone axis and the bonding with titanium has a shorter bond length, representing its 5-coordinate character.

Shown in Fig. 1 *D–F* are three electron diffraction patterns of a single crystalline JDF-L1 along the [001] zone axis, which were taken in our UEM. Diffraction spots for the pristine phase having unit cell dimensions of $a = b = 7.374$ Å, $c = 10.709$ Å were indexed based on the room temperature X-ray crystallographic data (29); some of the representative Miller indices are indicated in color. It has been reported that JDF-L1 gradually loses its water upon annealing at a temperature higher than 423 K, and this loss induces a shrinkage of the interlayer space along the *c*-axis direction perpendicular to the basal plane (28, 32). The dehydration process occurs slowly in the high vacuum of the microscope or when the specimen is heated by the laser; diffraction patterns of both structures are shown in Fig. 1. The hydrated form is known to be a good selective oxidation, single-site heterogeneous catalyst when

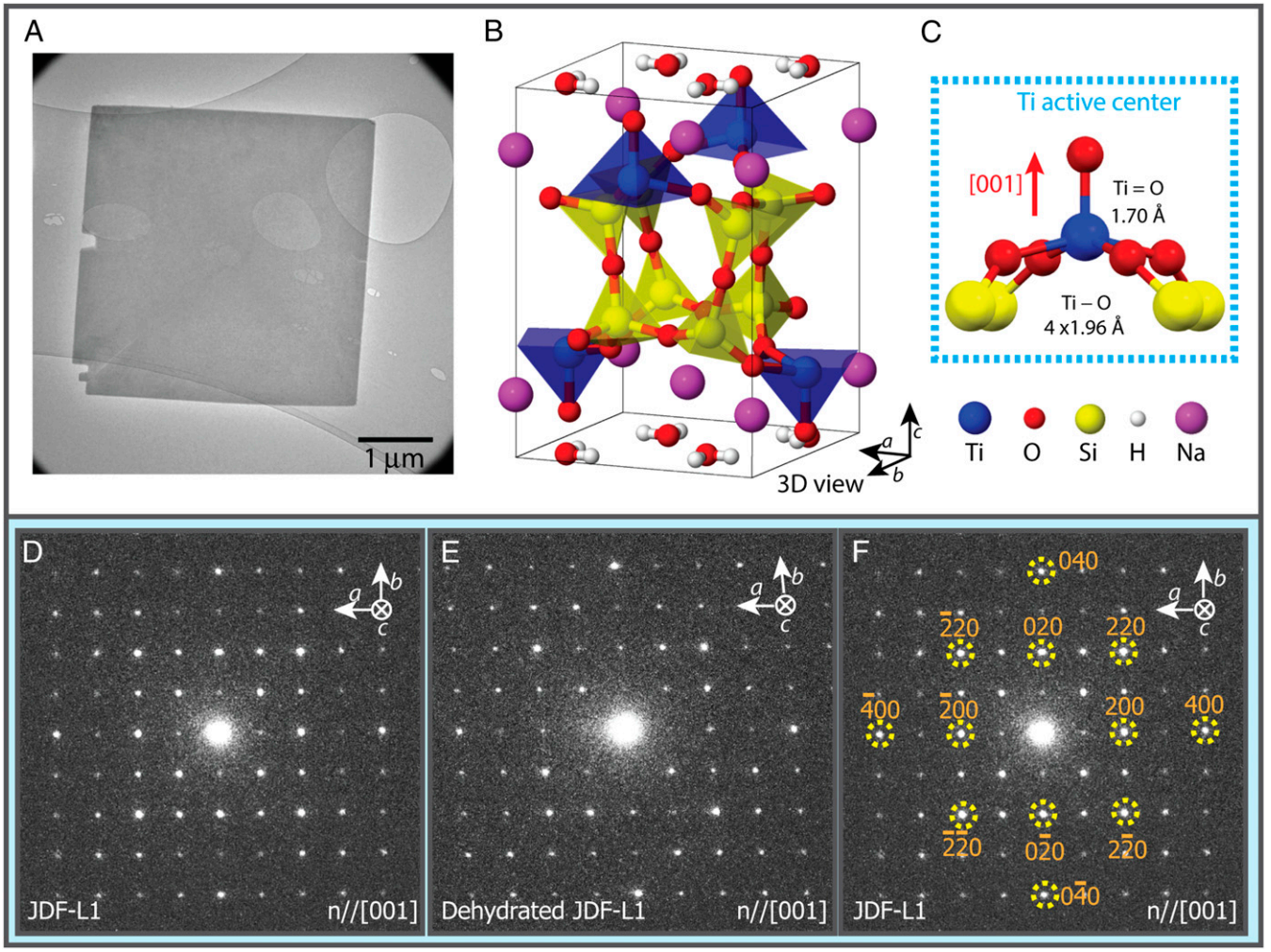

Fig. 1. Morphology, crystal structure, and the observed diffractions of JDF-L1. (*A*) Bright-field image of single crystal of JDF-L1; (*B*) 3D view of crystal structure of one unit cell. (*C*) Close up view of the 5-coordinated titanium at the catalytic active center. (*D–F*) Diffraction patterns of the pristine and dehydrated JDF-L1 obtained in our UEM. The diffraction peaks are indexed in the pattern for the pristine one.

pretreated with dilute HCl and H_2O_2 (27). Detailed comparison of the Bragg spots between the pristine and dehydrated JDF-L1 revealed a ~4% decrease for the interplanar distance of the pristine's (100) and (010) planes with a change in the angle between *a* and *b* axis from 90° to ~86.5°. This indicates that the loss of water causes not only the shrinkage of the interlayer space along the *c*-axis direction but also the structural change from the original tetragonal phase to a dehydrated phase with lower symmetry.

In our UEM studies, care was taken to follow such a dehydration effect and the sensitivity to radiation damage. An isolated single crystal with a typical size of about 3 × 3 μm was chosen by a selected-area aperture of 5 μm (Fig. 1*A*), and the thickness of the specimen was determined to be about 50 nm from our measured electron energy loss spectrum (EELS) (33) in the energy spectrometer of UEM. The initial excitation pulse (λ_i = 346 nm; typically 1 mJ/cm^2) is spatially and temporally in overlap at the specimen with the electron pulse, which is that of single-electron packets used in the stroboscopic mode of UEM. Time-resolved dynamics was obtained by varying the delay time between the two pulses while monitoring changes in the diffraction.

When the incident electron pulses are paralleled to the [001] zone axis, the Miller indices (*hkl*) for all of the observed Bragg spots have a zero value of *l* due to the Laue condition, and no change in the Bragg intensity or peak position was observed when the time delay was scanned up to several picoseconds after the photoexcitation. The patterns in Fig. 2 *A*–*C* were taken from different zone axes by tilting the sample stage, when two types of temporal behavior of diffraction intensity were observed. Bragg spots with $l = 0$ still show no significant temporal change, either in intensity or peak position. On the other hand, when $l \neq 0$, a femtosecond decay of the diffraction intensity with different amplitude was observed. The time dependency for the given Miller indices is given in Fig. 2*D*. To investigate the spatiotemporal behaviors of the specimen, diffraction intensity profiles at different times were constructed by fitting all Bragg spots to a Gaussian function. The time evolution has been fitted with a single-exponential decay and the fitted curves are designated by red and green solid lines.

The observed intensity change has a single-exponential decay time on the femtosecond time scale, as it is 350 fs from the fit of the transient in Fig. 2*D*; however, considering the repetitive scans taken, the range spans ±250 fs. One of the most significant finding of these studies is the selectivity found when "*l*" is nonzero. Examining spots for (201) and (200) planes, for example, we found ~15% decrease of intensity only from (201) planes, and not for the (200) planes. Following the femtosecond decay, the intensity remains unchanged up to several picoseconds and returns to equilibrium in less than 10 μs, as determined by our probing rate. The observed femtosecond dynamics is a consequence of the photoinduced transition without significant contribution from heating because of the time scale involved and based on the calculated structure factors and mean square displacements, as discussed below.

The intensity of a Bragg spot is affected by the motion of atoms within the unit cell. This is because the structure factor *F* and the intensity *I* of a Bragg spot (*hkl*) with a scattering factor ***S*** are determined by the position of atoms (***r***):

$$F(\boldsymbol{S}) = \sum_{k=1}^{N} n_k f_k(\boldsymbol{S}) \exp(-2\pi i(\boldsymbol{S}\cdot\boldsymbol{r}_k))$$

$$I(\boldsymbol{S}) \propto |F(\boldsymbol{S})|^2, \qquad [1]$$

where *N* is the number of atoms in the unit cell, n_k the occupancy factor of the *k*th atom, f_k is the scattering factor of the *k*th atom, $\boldsymbol{r}_k$ the position of the *k*th atom in the unit cell. From the inner products in Eq. **1**, the structure factor and hence the intensity of a spot (defined by ***S***) will only be affected by the atomic

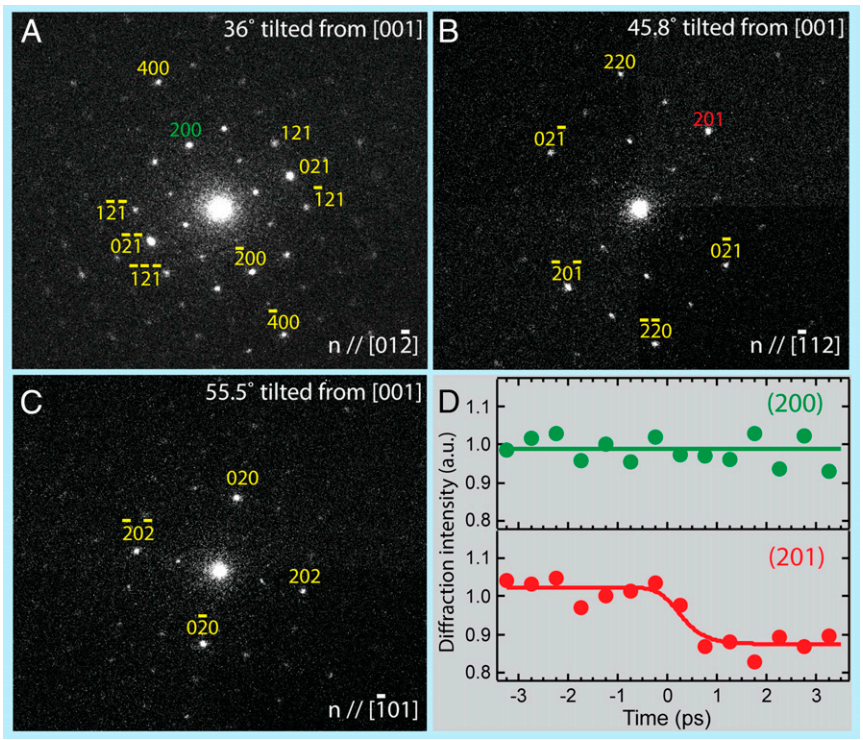

Fig. 2. Diffraction patterns at three different angles and time-dependent structural changes of JDF-L1. (*A*–*C*) Diffraction images observed at different zone axes before time 0; *n* is the electron direction. (*D*) Femtosecond intensity changes of (200) and (201) spots with time. Two different types of dynamics were observed: a decay with a femtosecond time constant (see main text) and another without a decay.

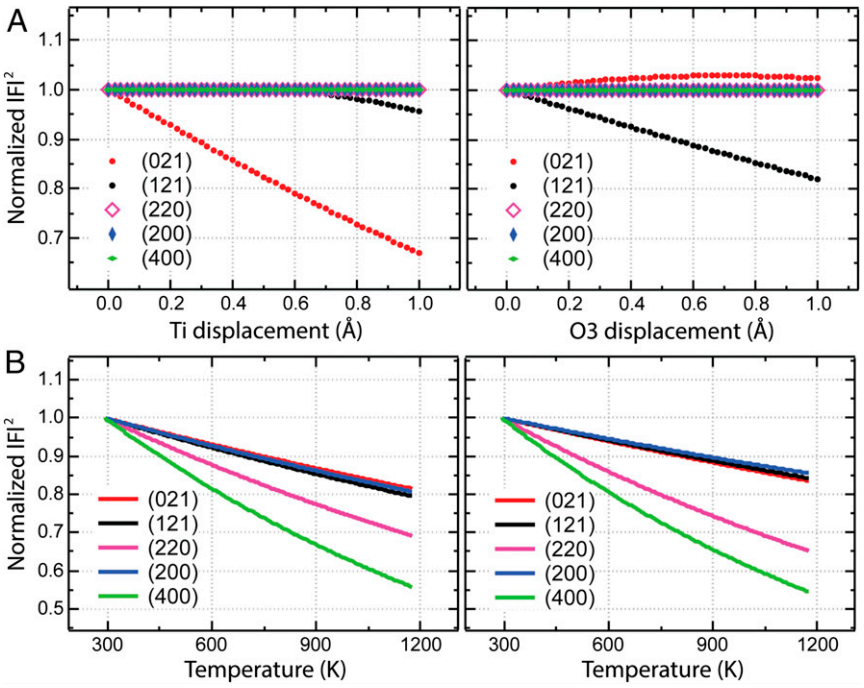

Fig. 3. (*A*) Influence of titanium and oxygen displacement on the structure factor. The displacement of Ti and O3 corresponds to the direction of Ti = O bond dilation. (*B*) Dependence of structure factor on temperature for isotropic (*Left*) and anisotropic (*Right*) atomic vibrations.

displacements with nonzero components in the corresponding Miller indices. Thus, the experimental fact that the temporal change of intensity was observed only for diffraction spots with a nonzero component of l indicates a structural change along the [001] direction.

The absorption of JDF-L1 at 346 nm (wavelength of the pump laser) has been assigned (34) to a ligand-to-metal charge transfer, from the O_{2p} orbital to the empty Ti_{3d} orbital. This transition to an antibonding state upon excitation weakens the bond and leads to its dilation along the Ti–O bond direction. As shown in Fig. 1*C*, among the five coordinated oxygen atoms around the central Ti, only the apical oxygen (O3) has a Ti = O double bond along the [001] direction. It follows that the dilation of the Ti = O double bond along the [001] causes the observed intensity change of Bragg spots with nonzero value of l.

To investigate the influence of atomic displacements on changes in diffraction intensity, we examined the structure factor when the Ti atom and the apical oxygen atom along the bond direction changes their equilibrium positions. The results in Fig. 3*A* were obtained with steps of 0.02 Å, and clearly show that only the diffraction intensity of spots with $l \neq 0$ is affected by the motion of Ti and the O3 atom along their bonding direction. The experimentally observed ∼15% intensity drop of (201) and ∼8% intensity drop of (121) correspond, respectively, to ca. 0.4-Å displacement of Ti and O3 in opposite directions, indicating a Ti–O bond length increase from 1.7 to ca. 2.5 Å, which is typical length for a Ti–O single bond (35). Here, we study localized single site expansion rather than a homogeneous crystal expansion, with the remained main crystal unchanged. That is why we did not observe reliable temporal change of the separation between conjugate Bragg peaks. These results reveal the femtosecond electron transfer induced by the photoexcitation at the catalytic active center of JDF-L1, and which occurs between the apical oxygen and the central Ti atom within the TiO_5 square-pyramid structure.

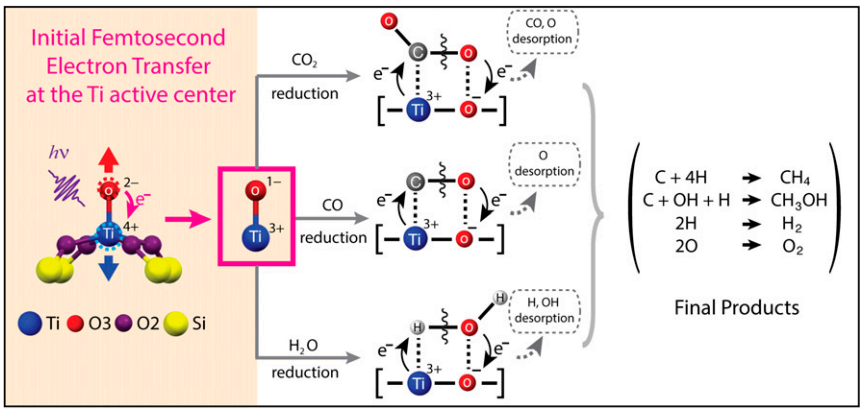

Fig. 4. Schematic illustration of the photocatalytic reduction of CO_2 and H_2O at the titanium active center, emphasizing the femtosecond laser induced electron transfer and subsequent Ti = O bond dilation.

The observed anisotropy of structural dynamics in diffraction, and its femtosecond time scale, suggests that the above process is a nonthermal one. However, if thermalization occurs, because of the destructive interferences and loss of the periodicity of atomic arrangements by thermal vibrations, it is of interest to consider the temperature effect on diffraction changes. The amplitude of the intensity change with temperature is usually described by the well-known Debye–Waller factor (36, 37). As reported elsewhere (26) in many studies (see, e.g., ref. 38), following femtosecond excitation, the electron–phonon coupling, which is on the time scale of a few picoseconds, leads to population of acoustic phonons and in this case a description of the change can be related to a rise in an effective temperature.

Following the discussion by Trueblood et al. (39), when the temperature effect on the diffraction intensity I of a Bragg reflection is taken into account, Eq. **1** can be modified as follows:

$$F(\boldsymbol{S}) = \sum_{k=1}^{N} n_k f_k(\boldsymbol{S}) D_k(\boldsymbol{S}) \exp(-2\pi i(\boldsymbol{S}\cdot\boldsymbol{r}_k)), \qquad [2]$$

where D_k ($\boldsymbol{S}$) is the Debye–Waller factor of the kth atom for the Bragg spot with a scattering factor $\boldsymbol{S}$. It is determined by the mean square displacement of the kth atom. When the atomic displacements are isotropic,

$$D(\boldsymbol{S}) = \exp\left[-2\pi^2 |S|^2 \langle u^2 \rangle\right], \qquad [3]$$

where $\langle u^2 \rangle$ is the isotropic mean square displacement of the atoms. When the atomic displacements are anisotropic, then:

$$D(\boldsymbol{S}) = \exp\left[-2\pi^2 \sum_{j=1}^{3}\sum_{l=1}^{3} h_j a^j U^{jl} a^l h_l\right], \qquad [4]$$

where h_1, h_2, h_3 are determined by the scattering vector $\boldsymbol{S}$, and a^1, a^2, a^3 are related to the basis vectors of the unit cell. The elements of the tensor U of order 3 are associated with the mean square displacements of the corresponding atom.

From Eqs. **2**–**4** one can see that the temperature effect on the structure factor F and the diffraction intensity I of a specific Bragg spot is determined solely by the amplitudes of mean square atomic displacements, either isotropic or anisotropic. It is of interest to explore the temperature dependence of these structure factors. However, this requires knowledge of the relationship of the amplitudes of atomic displacements to the temperature. In monoatomic systems, such as silicon, this relationship can be expressed using the Einstein model. With time dependence, following photoexcitation (38),

$$I(t) = I_0(t_-)\exp\left[-4\pi^2 |S|^2 u^2(t)\right]$$

$$u = \left[(\hbar/2\omega m)\coth\left(\hbar\omega/2k_B T_{\text{eff}}\right)\right]^{1/2}, \qquad [5]$$

where $I(t)$ is the measured intensity of a Bragg spot, $I_0(t_-)$ is the intensity before photoexcitation, u is the root mean square displacement of the atom with a mass of m, along each component of the 3D vector, $\hbar$ is the reduced Planck's constant, and k_B is the Boltzmann constant. T_{eff} is the effective temperature.

In our case here, Eq. **5** is not valid because we are dealing with a multiatomic system. Nevertheless if we make a bold approximation that all of the different atoms in JDF-L1 can be treated as independent and uncorrelated simple harmonic oscillators with the same angular frequency w; that the value of $\hbar\omega << 2k_B T$ for a temperature higher than 293 K; and that the experimentally determined effective mass m_{eff} can be used to measure the different atomic displacements for different atoms or the same type at different sites, one recovers the Einstein model with a simple relationship between the mean square atomic displacements of a specific atom and the effective temperature: $u^2 \propto T_{\text{eff}}$. Using the experimentally obtained, by Ferdov et al. (29), values of the isotropic and anisotropic mean square atomic displacements of JDF-L1 at 293 K, the structure factor dependence on the effective temperature for different Bragg spots were calculated. Similar results were obtained for the case of isotropic and anisotropic displacements as shown in Fig. 3*B*, where the calculated values for the decrease in amplitude for the spots (200) and (201) caused by the Debye–Waller effect are rather close to each other.

Based on the above discussion, the photocatalysis process, such as the photoreduction of CO_2 or H_2O by the JDF-L1 under UV light excitation may proceed according to the pathway given in Fig. 4. The photon excitation leads to electron transfer from the apical oxygen O3 to the center Ti atom, reducing the Ti^{4+} to the Ti^{3+} cation. Then the resulting Ti^{3+} ions react with the ambient CO_2 and H_2O, leading to their reduction and the formation of final products such as CH_4 and CH_3OH (40). The products noted in Fig. 4 are examples of consequences of electron transfer. Thus, the primary charge separation and its efficiency on the femtosecond time scale are critical for the subsequent chemistry of the catalytic process. Such primary charge transfer influence of reactivity has been realized for reactions of dative structures in solution (41) and in isolation (42).

In summary, by using 4D electron microscopy with high spatiotemporal resolution, we have captured the transient structure of the active site of a photoexcited catalytic process. It is demonstrated that following the photoexcitation, ultrafast electron transfer from the apical oxygen to the central Ti atom occurs nonthermally, as evident from the diffraction anisotropy, the time scale involved, and values of the structure factor. This transfer results in a separation of the titanium and the apical oxygen with a total displacement of up to ~0.8 Å, which indicates a transformation from the original Ti^{4+}=O^{2-} double bonding state to the dilated Ti^{3+}–O^{1-} single bonding one. The nature of bonding (double or triple) in metal oxides of this type has been elucidated by Gray and colleagues (43), but in the structure studied here the double and single bond characters of the 5-coordinated Ti^{4+} has been determined by X-ray methods (27, 29). Future extension of our technique to the visualization of the active sites at the atomic level on other various catalytic materials will be beneficial to the de novo design of specific catalysts with improved efficiency as well as the fundamental elucidation of mechanisms in such complex systems.

ACKNOWLEDGMENTS. We are grateful to Drs. Matthew E. Potter and Robert Raja for providing us with the JDF-L1 samples, and Prof. Harry Gray for helpful discussion. This work was supported by the National Science Foundation (DMR-0964886) and the Air Force Office of Scientific Research (FA9550-11-1-0055) in the Gordon and Betty Moore Center for Physical Biology at the California Institute of Technology. J.M.T. is grateful to the Kohn Foundation for financial support.

1. Williams LA, et al. (2013) Surface structural-chemical characterization of a single-site d^0 heterogeneous arene hydrogenation catalyst having 100% active sites. *Proc Natl Acad Sci USA* 110(2):413–418.
2. Stalzer MM, Delferro M, Marks TJ (2015) Supported single-site organometallic catalysts for the synthesis of high-performance polyolefins. *Catal Lett* 145(1):3–14.
3. Yang M, et al. (2015) A common single-site Pt(II)-O(OH)x- species stabilized by sodium on "active" and "inert" supports catalyzes the water-gas shift reaction. *J Am Chem Soc* 137(10):3470–3473.
4. Vilé G, et al. (2015) A stable single-site palladium catalyst for hydrogenations. *Angew Chem Int Ed Engl* 54(38):11265–11269.
5. Thomas JM (2015) Catalysis: Tens of thousands of atoms replaced by one. *Nature* 525(7569):325–326.
6. Kyriakou G, et al. (2012) Isolated metal atom geometries as a strategy for selective heterogeneous hydrogenations. *Science* 335(6073):1209–1212.
7. Flytzani-Stephanopoulos M (2014) Gold atoms stabilized on various supports catalyze the water-gas shift reaction. *Acc Chem Res* 47(3):783–792.

8. Yamashita H, Mori K (2007) Applications of single-site photocatalysts implanted within the silica matrixes of zeolite and mesoporous silica. *Chem Lett* 36(3):348–353.
9. Bellussi G, et al. (2012) ECS-3: A crystalline hybrid organic-inorganic aluminosilicate with open porosity. *Angew Chem Int Ed Engl* 51(3):666–669.
10. Maschmeyer T, Rey F, Sankar G, Thomas JM (1995) Heterogeneous catalysts obtained by grafting metallocene complexes onto mesoporous silica. *Nature* 378(6553): 159–162.
11. Dal Santo V, Liguori F, Pirovano C, Guidotti M (2010) Design and use of nanostructured single-site heterogeneous catalysts for the selective transformation of fine chemicals. *Molecules* 15(6):3829–3856.
12. Corma A (1997) From microporous to mesoporous molecular sieve materials and their use in catalysis. *Chem Rev* 97(6):2373–2420.
13. Yamashita H, Anpo M (2003) Local structures and photocatalytic reactivities of the titanium oxide and chromium oxide species incorporated within micro- and mesoporous zeolite materials: XAFS and photoluminescence studies. *Curr Opin Solid State Mater Sci* 7(6):471–481.
14. Yamashita H, et al. (1996) Photocatalytic decomposition of NO at 275 K on titanium oxides included within Y-zeolite cavities: The structure and role of the active sites. *J Phys Chem* 100(40):16041–16044.
15. Bellussi G, Carati A, Clerici MG, Maddinelli G, Millini R (1992) Reactions of titanium silicalite with protic molecules and hydrogen-peroxide. *J Catal* 133(1):220–230.
16. Takeuchi M, Sakai S, Ebrahimi A, Matsuoka M, Anpo M (2009) Application of highly functional Ti-oxide-based photocatalysts in clean technologies. *Top Catal* 52(12): 1651–1659.
17. Anpo M, Thomas JM (2006) Single-site photocatalytic solids for the decomposition of undesirable molecules. *Chem Commun (Camb)* 31(31):3273–3278.
18. Dhakshinamoorthy A, Navalon S, Corma A, Garcia H (2012) Photocatalytic CO_2 reduction by TiO_2 and related titanium containing solids. *Energy Environ Sci* 5(11): 9217–9233.
19. Grätzel M (2001) Photoelectrochemical cells. *Nature* 414(6861):338–344.
20. Maeda K, Domen K (2010) Photocatalytic water splitting: Recent progress and future challenges. *J Phys Chem Lett* 1(18):2655–2661.
21. Anpo M, Takeuchi M (2003) The design and development of highly reactive titanium oxide photocatalysts operating under visible light irradiation. *J Catal* 216(1-2): 505–516.
22. Takeuchi M, Dohshi S, Eura T, Anpo M (2003) Preparation of titanium-silicon binary oxide thin film photocatalysts by an ionized cluster beam deposition method. Their photocatalytic activity and photoinduced super-hydrophilicity. *J Phys Chem B* 107(51): 14278–14282.
23. Ampelli C, Perathoner S, Centi G (2015) CO_2 utilization: An enabling element to move to a resource- and energy-efficient chemical and fuel production. *Phil Trans R Soc A* 373(2037):20140177.
24. Zewail AH (2010) Four-dimensional electron microscopy. *Science* 328(5975):187–193.
25. Zewail AH, Thomas JM (2010) *4D Electron Microscopy: Imaging in Space and Time* (Imperial College Press, London).
26. Zewail AH (2014) *4D Visualization of Matter* (Imperial College Press, London).
27. Roberts MA, et al. (1996) Synthesis and structure of a layered titanosilicate catalyst with five-coordinate titanium. *Nature* 381(6581):401–404.
28. Kostov-Kytin V, Mihailova B, Ferdov S, Petrov O (2004) Temperature-induced structural transformations of layered titanosilicate JDF-L1. *Solid State Sci* 6(9):967–972.
29. Ferdov S, et al. (2007) Refinement of the layered titanosilicate AM-1 from single-crystal X-ray diffraction data. *Acta Crystallogr Sect E Crystallogr Commun* 63:I186.
30. Barwick B, Park HS, Kwon OH, Baskin JS, Zewail AH (2008) 4D imaging of transient structures and morphologies in ultrafast electron microscopy. *Science* 322(5905): 1227–1231.
31. Barwick B, Flannigan DJ, Zewail AH (2009) Photon-induced near-field electron microscopy. *Nature* 462(7275):902–906.
32. Du HB, Chen JS, Pang WQ (1996) Synthesis and characterization of a novel layered titanium silicate JDF-L1. *J Mater Chem* 6(11):1827–1830.
33. Egerton R (2011) *Electron Energy-Loss Spectroscopy in the Electron Microscope* (Springer Science & Business Media, New York).
34. Gao XT, Bare SR, Fierro JLG, Banares MA, Wachs IE (1998) Preparation and in-situ spectroscopic characterization of molecularly dispersed titanium oxide on silica. *J Phys Chem B* 102(29):5653–5666.
35. Thomas JM, Sankar G (2001) The role of XAFS in the in situ and ex situ elucidation of active sites in designed solid catalysts. *J Synchrotron Radiat* 8(Pt 2):55–60.
36. Debye P (1913) Interferenz von röntgenstrahlen und wärmebewegung. *Ann Phys* 348(1):49–92.
37. Waller I (1923) Zur frage der einwirkung der wärmebewegung auf die interferenz von röntgenstrahlen. *Z Phys* 17(1):398–408.
38. Yurtsever A, Zewail AH (2009) 4D nanoscale diffraction observed by convergent-beam ultrafast electron microscopy. *Science* 326(5953):708–712.
39. Trueblood KN, et al. (1996) Atomic displacement parameter nomenclature - Report of a subcommittee on atomic displacement parameter nomenclature. *Acta Crystallogr A* 52:770–781.
40. Mori K, Yamashita H, Anpo M (2012) Photocatalytic reduction of CO_2 with H_2O on various titanium oxide photocatalysts. *Rsc Adv* 2(8):3165–3172.
41. Steiger B, Baskin JS, Anson FC, Zewail AH (2000) Femtosecond dynamics of dioxygen-picket-fence cobalt porphyrins: Ultrafast release of O_2 and the nature of dative bonding. *Angew Chem* 112(1):263–266.
42. Zhong D, Zewail AH (1999) Femtosecond dynamics of dative bonding: concepts of reversible and dissociative electron transfer reactions. *Proc Natl Acad Sci USA* 96(6): 2602–2607.
43. Winkler J, Gray H (2012) Electronic structures of oxo-metal ions. *Molecular Electronic Structures of Transition Metal Complexes I, Structure and Bonding* (Springer, Berlin Heidelberg)17–28.